Nanoscale

Diversity of physical properties of bacterial extracellular membrane vesicles revealed through atomic force microscopy phase imaging

Journal:	*Nanoscale*
Manuscript ID	NR-ART-12-2019-010850.R1
Article Type:	Paper
Date Submitted by the Author:	20-Mar-2020
Complete List of Authors:	Kikuchi, Yousuke; Kanazawa University, Institute of Science and Engineering Obana, Nozomu; University of Tsukuba, Transborder Medical Research Center, Faculty of Medicine; University of Tsukuba, Microbiology Research Center for Sustainability (MiCS) Toyofuku, Masanori; University of Tsukuba, Microbiology Research Center for Sustainability (MiCS); University of Tsukuba, Faculty of Life and Environmental Sciences Kodera, Noriyuki; Kanazawa University, Nano Life Science Institute (WPI-NanoLSI) Soma, Takamitsu; University of Tsukuba, Graduate School of Life and Environmental Sciences ANDO, TOSHIO; Kanazawa University, Nano Life Science Institute (WPI-NanoLSI) Fukumori, Yoshihiro; Kanazawa University, Nano Life Science Institute (WPI-NanoLSI); Kanazawa University, Vice President Nomura, Nobuhiko; University of Tsukuba, Microbiology Research Center for Sustainability (MiCS); University of Tsukuba, Faculty of Life and Environmental Sciences Taoka , Azuma ; Kanazawa University, Institute of Science and Engineering; Kanazawa University, Nano Life Science Institute (WPI-NanoLSI)

ARTICLE

Diversity of physical properties of bacterial extracellular membrane vesicles revealed through atomic force microscopy phase imaging †

Received 00th January 20xx,
Accepted 00th January 20xx

DOI: 10.1039/x0xx00000x

Yousuke Kikuchi,[a] Nozomu Obana,[b,c] Masanori Toyofuku,[c,d] Noriyuki Kodera,[e] Takamitsu Soma,[f] Toshio Ando,[e] Yoshihiro Fukumori,[e,g] Nobuhiko Nomura ‡ [#c,d] Azuma Taoka ‡ [#a,e]

Bacteria release nanometer-scale extracellular membrane vesicles (MVs) to mediate a variety of biological processes. We analyzed individual MVs under physiological conditions by phase imaging of high-speed atomic force microscopy to assess the physiological heterogeneity of MVs isolated from bacterial cultures. The phase imaging makes it possible to map the physical properties of an individual, fragile MV in an isolated MV population containing a broad variety of vesicle diameters, from 20 to 150 nm. We also developed a method for quantitatively comparing the physical properties of MVs among samples. This allowed for the comparison of the physical properties of MVs isolated from different bacterial species. We compared the bacterial MVs isolated from four bacterial species and artificially synthesized liposomes. We demonstrate that each bacterial species generates physically heterogeneous types of MVs, unlike the physical homogeneity displayed by liposomes. These results indicate that the physical heterogeneity of bacterial MVs are caused by mainly compositional differences mediated through biological phenomena and could be unique to each species. We provide a new methodology using the phase imaging that would pave the way for single-vesicle analysis of extracellular vesicles of broad size range.

Introduction

Extracellular nanometer-scale vesicles that consist of lipid membrane are extensively involved in cellular processes in all domains of life:[1] Eukariya,[2] Archaea,[3] and Bacteria.[4–6] These vesicles deliver chemical and genetic cargoes from donor to recipient cells. Eukaryotic extracellular vesicles, known as exosomes, attract particular attention from various life science fields, including medicine, pharmacology, and cancer biology.[7,8] Bacteria are also known[9] to release extracellular vesicles termed as membrane vesicles (MVs) with diameters of 20 to 400 nm.[4–6] To date, increasingly frequent publications indicate that MVs play multiple roles in biological processes, e.g., transport of virulence factors, lateral gene transfer, interception of bacteriophages, antibiotic and eukaryotic defence factors, cell detoxification, and bacterial cell-to-cell communication.[4–6] Moreover, bacterial MVs serve as platforms for nanobiotechnology, e.g., drug delivery, vaccines, and enzyme transport.[10]

Interestingly, evidences continue to accumulate, suggesting heterogeneity of bacterially released MVs. Several types of MVs, differing in structure and composition, have been reported[11]. In addition, different routes for MV formation are reported.[11] At least two fundamentally distinct routes, endolysin-triggered cell lysis[12] and membrane blebbing[4] are reported in Gram-negative bacteria. The MV heterogeneity may contribute to the diverse MV functions. Notably, a single MV can deliver a quantity of chemical signal molecules sufficient to modify the metabolism of a recipient cell,[13] suggesting that a single MV is enough to achieve the required function. Based on these indications, much remains to be learned about MV functions and mechanisms by measuring and characterizing MVs at a single particle level in heterogeneous MV populations. To date, most of the MV studies cope with a heterogenous MV population that would level out the function of each MV particles. Towards a better understanding of MVs, developments of new methods are required that would enable us to characterize each particle.

Atomic force microscope (AFM) has multifunctional imaging modes that allow the measurement of various physiochemical properties of biological specimens at nanometer-scale resolution.[14] Herein the present study, we employed AFM phase imaging for a quantitative characterization of physical

[a] Institute of Science and Engineering, Kanazawa university, Kakuma-machi, Kanazawa, Ishikawa 920-1192, Japan
[b] Transborder Medical Research Center, Faculty of Medicine, University of Tsukuba, 1–1–1 Tennodai, Tsukuba, Ibaraki 305-8572, Japan
[c] Microbiology Research Center for Sustainability (MiCS), University of Tsukuba, 1-1-1 Tennoudai, Tsukuba, Ibaraki 305-8572, Japan
[d] Faculty of Life and Environmental Sciences, University of Tsukuba, 1–1–1 Tennodai, Tsukuba, TARA center, Ibaraki 305-8572, Japan
[e] Nano Life Science Institute (WPI-NanoLSI), Kanazawa University, Kakuma-machi, Kanazawa, Ishikawa 920-1192, Japan
[f] Graduate School of Life and Environmental Sciences, University of Tsukuba, 1-1-1 Tennodai, Tsukuba, Ibaraki 305-8572, Japan
[g] Vice President, Kanazawa University, Kakuma-machi, Kanazawa, Ishikawa 920-1192, Japan
nomura.nobuhiko.ge@u.tsukuba.ac.jp, aztaoka@staff.kanazawa-u.ac.jp
†Electronic Supplementary Information (ESI) available: [details of any supplementary information available should be included here]. See DOI: 10.1039/x0xx00000x
‡ Equal contribution.

properties of individual MVs within heterogeneous MV populations under physiological buffer conditions. A phase imaging in amplitude modulation AFM can image compositional variations in heterogeneous surfaces by detecting phase difference between the exciting signal and the cantilever oscillation.[15–18] A given phase difference, expressed as a phase-shift degree, is attributed to the energy dissipation from a scanning tip onto a sample surface during AFM imaging.[19,20] Because the intensity of the energy dissipation from the scanning tip is influenced by physical properties of the scanned sample surface, such as adhesion, elasticity, and friction, AFM phase imaging allows mapping of compositional differences across the sample surface. AFM phase imaging is frequently used in the fields of surface science and materials science as a powerful tool for examining compositional variations on heterogeneous abiotic surfaces.[16,17,21] However, this technique has rarely been applied to biological specimens, largely due to the potential for damage to the sample while imaging under physiological conditions. The lipid membrane vesicle is among the most fragile of biological materials. To overcome this limitation, we used high-speed AFM, which was developed for imaging of soft biological specimens in liquid.[22] High-speed AFM does less damage to samples during imaging because the constant force from the probe to the sample amounts to a maximum of ~100 pN.[22] High-speed AFM has leveraged this advantage to offer new insights into nanometer-sized biomolecules, such as proteins, lipid bilayers, and living cells under physiological conditions.[23–25]

We developed a method for a quantitative measurement of the physical properties of bacterial MVs under high-speed AFM phase mode. We assessed MV physical diversity in bacterial MV populations isolated from three Gram-negative and one Gram-positive bacterial species: *Escherichia coli*, *Pseudomonas aeruginosa*, *Paracoccus denitrificans*, and *Bacillus subtilis*. Our results reveal that a single bacterial species generates heterogeneous types of MVs. Moreover, these MV physical parameters exhibited species-specific patterns. Our results reveal a previously unrecognized physical diversity of bacterial MVs.

Experimental

Bacterial strains and growth conditions

E. coli RN102,[26] *P. aeruginosa* PAO1,[27] and *P. denitrificans* Pd1222[28] were used in this study. To omit flagella from MV samples in *B. subtilis* 168,[29] a flagella mutant (*B. subtilis* 168 *Δhag* (P_{xylA})) was constructed as follows. Approximately 500 bp of flanking regions upstream and downstream of the hag gene were amplified from the *B. subtilis* 168 genome by PCR using the primer sets hag-N5 (AGAGCCATTTGAAAAGTCTACTGC)/hag-N3(AGATCTCCATATAATTTTTGTGTTTTGTTCCTCCCTGAAT) and hag-C5 (ACTTTAATTTAGTGAAGCTTTTTTAAAAAAGACCTTGGCG)/hag-3(CTACAAATAACCCAAGAAATTCAG). Spectinomycin-resistant gene SpcR was amplified from the *B. subtilis* TMO310[30] genome by PCR using the primer set spc-Fw(ATTCAGGGAGGAACAAAACACAAAAATTATATGGAGATCT)/spc-Rv(CGCCAAGGTCTTTTTTAAAAAAGCTTCACTAAATTAAAGT). The upstream and downstream fragments of the hag gene and the antibiotic gene cassette were ligated by overlap PCR using the primer set hag-N5(AGAGCCATTTGAAAAGTCTACTGC)/hag-C3(AGACCTGTTATTCTTGTGACCATC). The resulting DNA fragments were transformed into *B. subtilis* 168 (P_{xylA}).[31] The deletion of the target gene was confirmed by PCR and sequencing.

To isolate MVs, we grew these bacteria aerobically at 200 rpm at 37 °C until the stationary phase. *E. coli* were cultured in a Luria–Bertani medium for 16 h. *P. denitrificans* were cultured in a tryptic soy broth (TSB) medium for 16 h. *P. aeruginosa* were cultured in a TSB medium for 24 h. *B. subtilis* were cultured in a brain heart infusion medium for 24 h.

MV isolation and quantification

Cell cultures were centrifuged for 10 min at 6,000g at 4 °C. The supernatant was filtered through a polyvinylidene difluoride filter of pore size 0.45 μm (Merck Millipore, Germany). The filtered spent media were ultracentrifuged for 1 h at 150,000g at 4 °C. MVs were precipitated as pellets. The obtained pellets were resuspended in phosphate-buffered saline (PBS). The resuspended MVs of *P. denitrificans* were used for AFM and TEM observations. For further MV purification, the MVs of *E. coli*, *P. aeruginosa*, and *B. subtilis* were purified using density-gradient centrifugation in an iodixanol (Optiprep, Axis-Shield, Scotland) gradient of 45%–10% as described previously,[12,31] and resuspended in PBS. The resuspended MVs of *E. coli* and *P. aeruginosa* were used for AFM and TEM observations. *B. subtilis* culture contained large amount of extracellular DNA which are released from dying cells[31]. To remove the extracellular DNA, the MV fraction of *B. subtilis* was further treated with 0.5 U DNase I for 30 min at 37 °C. DNase I was then removed by ultracentrifugation, and the MVs were resuspended in PBS. MVs were quantified using the membrane-staining fluorescent dye FM4-64 and a Varioskan flash fluorimeter (Thermo Scientific, USA), as previously explained.[12,31]

Liposome preparation

Liposomes were prepared from *E. coli* lipid extract (Avanti Polar Lipid, USA). The *E. coli* lipid extract (10 mg) was dissolved in 1.6 ml chloroform and transferred in a glass vial. The organic solvent was removed using a dry nitrogen stream. The obtained dried lipid film was suspended in 5 ml Tris–NaCl/EDTA buffer (10 mM Tris–NaCl, 0.1 M NaCl, 0.1 mM EDTA (pH 7.5)). The suspension was then incubated at room temperature for 16 h. Once the lipids were hydrated, the suspension was treated in a bath sonicator for 10 min to produce unilamellar vesicles. The aggregated lipids were removed by centrifugation at 6,000g for 15 min and filtration through membrane filters of pore size 0.45 μm. The filtered solution was ultracentrifuged at 150,000g for 1 h at 4 °C, and the pellet was then resuspended in PBS and used for AFM observation.

Transmission electron microscopy

To prepare the specimen for TEM observation, a Formvar and carbon-coated copper grid (JEOL, Japan) was placed on a drop of MV suspension for about 1 min. The grids were negatively stained with 2% uranyl acetate for several seconds. The specimens were studied with a TEM JEM 2000EX (JEOL, Japan) TEM operating at 120 kV in bright-field mode.

AFM observation

We used a laboratory-built, tapping-mode, high-speed AFM apparatus.[22] For phase imaging, the phase shift between the cantilever oscillation and the excitation signal was detected using a HF2LI lock-in-amplifier (Zurich Instruments, Switzerland). The lock-in-amplifier measures the phase shift from averaged multiplication of excitation and oscillation signals over one period. Due to a time delay in the detection of the phase-shift mechanism, adhesion force between the cantilever tip and sample surface is the one that most affects the phase-shift value.[32]

The probe tip was grown on the top of the cantilever by electron beam deposition using an electron beam lithography system (ELS-7500UK, Elionix, Japan). The deposition time was 90 s. The tapping setup used a small silicon nitride cantilever (BL-AC10-DS, Olympus, Japan) with a spring constant k of ~0.1 N/m and a resonance frequency f of ~400–500 kHz in water. The free-oscillation peak-to-peak amplitude of the cantilever was set to 2 nm, and the amplitude set point was at 1.7 nm. The tapping force was optimized for phase imaging without damage to MVs. The tapping force was about 50 pN during AFM imaging.

AFM sample preparation

MVs were immobilized on a silanized mica surface for AFM observation. For the silanization of the mica surface, we deposited 3 µl of 3-aminopropyltriethoxysilane (APTES) (Shin-Etsu Chemical, Japan) solution on the freshly cleaved mica and incubated it for 3 min in the moist chamber. The APTES concentrations were 0.03%, 0.05%, 0.02%, and 0.0001% for *P. denitrificans*, *P. aeruginosa*, *E. coli*, and *B. subtilis* MVs, respectively (Fig. S1). The 0.02% APTES solution was used for liposome observation. After silanization, we washed the mica surface three times with 20 µl ultrapure water and then three times with 20 µl PBS. The MV suspension was then added onto the mica and incubated for 15 min at room temperature. The concentrations of *P. denitrificans*, *P. aeruginosa*, *E. coli*, and *B. subtilis* MV suspensions were 5, 5, 10, and 20 ng protein/µl, respectively. After incubation, excess MVs were removed by washing three times with 20 µl PBS. PBS (65 µl) was used as the immersive imaging buffer. All AFM observations were performed at room temperature. For *E. coli* MVs, *P. aeruginosa* MVs, *P. denitrificans* MVs, and liposome observations, AFM images were recorded at 2 s/frame in a scanning area of 400 × 400 nm with 200 × 200 pixels. For *B. subtilis* MVs observations, AFM images were recorded at 5 s/frame in a scanning area of 800 × 800 nm with 400 × 400 pixels. The scanning area, the scanning speed and the number of pixels were optimized to capture about twenty to fifty MV particles and/or at least three polystyrene beads in a single AFM image. Processive AFM imaging of *P. aeruginosa* MVs was recorded at 0.5 s/frame in a scanning area of 200 × 200 nm with 100 × 100 pixels.

Polystyrene beads which are 50 nm in diameter (PolyScience, USA) were used as an internal standard of phase-shift degree. These polystyrene beads were mixed with the MVs sample at a proportion of ~0.005% of sample volume and loaded on the mica surface together with the MVs. Carboxylate polybeads which are 50 nm in diameter (PolyScience, USA) were used for estimating the effect of APTES concentration on the phase-shift value.

Image analysis

Images were processed using ImageJ software (National Institutes of Health, USA). We applied a flattening filter to the topographic and phase images to remove the substrate-tilt effect using the "fit polynomial" plugin. MV diameters were measured from peak heights of each MV particles in AFM images. To adjust the phase-shift degree of the mica substrate to 0, we subtracted the averaged values of the phase-shift degree at the mica substrate from the phase image. Linear adjustments to signal contrast and brightness were made in the images presented, but no gamma settings were changed. The topographic and phase images were merged using the "merge channels" command in ImageJ. The phase-shift degree obtained at the top of each MV, liposome, or polystyrene bead was used in order to avoid artifacts from parachuting. The positions of the tips were obtained by measuring the "max grey value" of each particle using the "measure" command in ImageJ.

Normalization of the phase-shift value

The normalized phase-shift values (ϕ_{cal}) for MV particles, liposomes, and polystyrene beads were calculated by dividing the phase-shift degree of those particles by the averaged phase-shift degree of polystyrene beads (ϕ_{bead}) in the same phase image. ϕ_{cal} values were calculated from phase-shift images containing at least three polystyrene beads.

MV physical property mapping

Physical property mapping of MVs was performed by AFM phase imaging. The tapping force was set to 50 pN throughout all experiments. Energy dissipation was measured from the phase difference between a cantilever oscillation and a sinusoidal reference signal. The phase difference is expressed as the phase-shift degree. A large value of the phase-shift degree indicates high energy dissipation by high adhesion, elasticity, and/or friction on a sample surface. Notably, it has been reported that the main source of the phase shift, which is observed using the carbon tip in liquid as our experimental setting, is the dissipative adhesion forces between the tip and the sample surface.[32]

Statistical analysis

Significant differences between a pair of ϕ_{cal} distributions were estimated using the χ-square test because ϕ_{cal} distributions of bacterial MVs did not fit to a Gaussian curve. First, one set of data was used as the reference data, and the other set of data was the observed data. Then, the class for which both the

frequency values of the reference data and the observation values were greater than 2 was used to calculate the χ-square value. We calculated the p-value from the obtained χ-square using the "CHISQ.DIST.RT" formula in Microsoft Excel. In this study, p-values below 0.005 were considered statistically significant.

Results

AFM imaging of bacterial MVs

We observed MVs produced from three Gram-negative bacteria belonging to Phylum Proteobacteria: *E. coli* K-12 derivative,[26] *P. aeruginosa* PAO1,[27] and *P. denitrificans* Pd1222.[28] We also observed MVs produced from one Gram-positive bacterium belonging to Phylum Firmicutes: *B. subtilis* 168.[29] MVs were isolated from the spent media of each stationary phase bacterial culture by filtration and gradient ultracentrifugation, as described in the experimental section. The purity and intactness of the MVs were assessed by TEM observation of the negatively stained samples (Figs. S2a–d). Although most MVs appeared to be intact spherical structures, some fragmented membranous structures appeared to be collapsed vesicles. Thus, for the analysis in this study, we considered a symmetric spherical vesicle to be an intact MV during microscopic observations using AFM and TEM.

Figure 1 presents topographic AFM images of MVs isolated from the four bacterial species. All MVs exhibited similar smooth spherical structures with no protrusions or patterns on their surfaces (Figs. 1a–d). The distributions of MV diameters measured by AFM were compared with those measured by TEM (Figs. 1e–f). MV diameters were measured from heights of MV particles in AFM images. The diameter distributions from AFM and TEM images overlapped in the MV sample of each of the four bacterial species. The average MV diameters from TEM images were slightly larger (by ~8% on average) than those from AFM images across all species. These differences were likely due to differences in dehydrated and hydrated sample states. Broadly, these results indicate that all MV sizes contained in the samples were successfully imaged by AFM. Thus, an evaluation of the collective distribution of MV properties in the sample could be achieved by AFM imaging under the optimized conditions in this study.

The concentrations of APTES solutions used for the silanization of mica substrates were critical for imaging intact MVs by AFM (Fig. S1a). When the mica was treated with an insufficient APTES concentration, only a small number of blurred MVs were observed on the mica substrate (Fig. S1a). This outcome was the result of the weak adsorption of MVs onto the substrate. In contrast, when the mica was treated with an excessive APTES concentration, circular sheet-like structures with a thickness of 5 to 6 nm were observed instead of spherical vesicles (Fig. S1a). These sheet-like structures dissolved upon the addition of Triton X-100 surfactant during high-speed AFM observations, indicating that the sheet-like structures were lipid bilayer membranes (Fig. S1b). Excessive APTES may thus cause the collapse of vesicles by extreme binding forces on the mica substrate. Interestingly, the optimal APTES concentration differed among bacterial species (Fig. S1c). The optimal APTES concentrations for observing *E. coli*, *P. aeruginosa*, *P. denitrificans*, and *B. subtilis* MVs were 0.02%, 0.05%, 0.03%, and 0.0001%, respectively. The MV size distributions measured from the AFM images and the TEM images clearly overlapped (Fig. 1e-h), indicating that the above APTES concentrations had no adverse effect on the measurements. Furthermore, the difference in the optimal APTES concentrations suggest that electrostatic properties of MV surfaces are species-specific.

Imaging of physical properties of MVs using AFM phase mode

Figure 2 presents topographic images (Fig. 2, Column i), phase images (Fig. 2, Column ii), and merged topographic and phase images (Fig. 2, Column iii) of MVs from cultures of the four bacterial species. The topographic and phase images were acquired simultaneously. The color in the merged image represents the ratio of the height and phase-shift degree of an individual MV. In the merged image, red indicates a non-adherent/hard MV, which has low adhesion, elasticity, and/or friction. In contrast, green indicates an adherent/soft MV, which has high adhesion, elasticity, and/or friction. Consequently, in the merged images, MVs from all four bacterial species are represented as a variety of colored spheres (e.g., orange-, yellow-, and green-colored spheres; Fig. 2, Column iii), indicating that the MV population produced by each of these bacteria has diverse physical properties.

To assess whether the phase-shift degrees measured from MVs are static or change dynamically during imaging, sequential phase images of *P. aeruginosa* MVs were recorded for 60 s (0.5 s/frame) (Supplementary Movie S1). The time series of the phase-shift degrees at the tips of the four MVs in Mov. S1 are presented in Fig. S3. The phase-shift degrees of the four MVs were almost constant, indicating that the phase shift of the MVs was stable during observation. Thus, the physical properties observed by the AFM phase mode revealed the intrinsic, static nature of each MV. This finding constitutes the first demonstration of the physical heterogeneity of MV particles produced by a single bacterial species.

Quantitative analysis of MV physical properties

Figure 3a presents a merged image of the topographic and phase images (Fig. S4a) obtained from the mixture of *P. aeruginosa* MVs and polystyrene beads. The phase-shift degree at the top of each MV particle and polystyrene bead was measured to exclude artifacts from cantilever parachuting (i.e. complete detachment of the cantilever tip from the sample surface at a downhill region of the MV/polystyrene bead) (Figs. 3b and S5). The normalized phase-shift value (ϕ_{cal}) was defined as the quotient of the obtained phase-shift degree from an MV particle (ϕ_{MV}) and the average phase-shift value from polystyrene beads (ϕ_{bead}) from the same phase image (Fig. 3b). Figure S4b presents ϕ_{MV}, ϕ_{bead}, and ϕ_{cal} calculated from the phase-shift image of Fig. 3a. Non-adherent/hard MVs had low ϕ_{cal} values, whereas adherent/soft MVs had high ϕ_{cal} values. The ϕ_{cal} of polystyrene beads was 1, whereas the ϕ_{cal} of mica

was 0. The ϕ_{cal} values of MVs varied widely, ranging from 1 to 3 (Fig. S4b).

In order to successfully prepare specimens for analysis for each species, the APTES concentration used for mica silanization differed depending on bacterial species. We measured the ϕ_{cal} values of carboxylate polybeads on mica substrates treated with 0.02%, 0.05%, 0.03%, and 0.0001% APTES. The differences in APTES concentrations had no effects on ϕ_{cal} values of the beads (Fig. S6), indicating that APTES concentration is not expected to affect ϕ_{cal} values.

The reproducibility of ϕ_{cal} values between experiments was confirmed. The ϕ_{cal} values of polystyrene beads, which were measured in independent experiments using different tips and mica substrates, were constant at 1.00 ± 0.06 (n = 62). The aliquots of the *P. aeruginosa* MV sample were independently measured three times (Fig. 3c). No significant differences were observed between the detected distributions using the χ-square test (p = 0.5–0.7), demonstrating the reproducibility of ϕ_{cal} value measurements. *P. aeruginosa* MV ϕ_{cal} values were widely distributed from 1 to 3 (Fig. 3d). The distribution was not random but instead consisted of two peaks: a narrow peak with a vertex at ϕ_{cal} = 2.6 and a broad peak between ϕ_{cal} values of 1 and 2. This result suggests at least two groups of MVs with different physical properties present in the *P. aeruginosa* MV population. The reproducibility of the ϕ_{cal} value distribution in biological replicates was also confirmed. The ϕ_{cal} distributions of two *P. denitrificans* MV samples isolated from independent cultures demonstrated no significant differences (χ-square p = 0.3; Fig. S7). Thus, we have no reason to doubt that the physical diversity of MVs can be quantitatively assessed and compared among bacterial species using the ϕ_{cal} value.

MV physical heterogeneity caused by biological factors

The ϕ_{cal} distribution of *E. coli* MVs was compared with that of artificially synthesized liposomes made from *E. coli* lipid extracts. There was no correlation between the ϕ_{cal} values and diameters of vesicles either in *E. coli* MVs (Fig. 4a) or in liposomes (Fig. 4b). This finding suggests that particle size does not affect the physical properties measured by phase shift. ϕ_{cal} distributions clearly differed between *E. coli* MVs and liposomes (Figs. 4c,d). The *E. coli* MV ϕ_{cal} distribution ranged from 1.5 to 4.5, with three broad peaks at 2.4, 3.4, and 4.2 (Fig. 4c). In contrast, the liposome ϕ_{cal} distribution revealed a single peak at 2.4. The *E. coli* MVs ϕ_{cal} distribution failed to fit a Gaussian curve ($p < 0.005$), whereas the Gaussian curve did not fail to fit the liposome ϕ_{cal} distribution (p = 0.93). These results indicate that the *E. coli* lipid liposomes were physically homogeneous, in contrast to the *E. coli* MVs, and that the physical heterogeneity of MVs was caused not by the geometric characteristics of the vesicle lipid but rather by compositional differences mediated through biological phenomena.

Species-dependent physical properties of MVs

The MV ϕ_{cal} distributions from the four bacterial species *E. coli*, *P. aeruginosa*, *P. denitrificans*, and *B. subtilis* were compared (Figs. 5a–d). Each bacterial species' MV ϕ_{cal} distribution was heterogeneous. The ϕ_{cal} distributions significantly differed among bacterial species ($p < 1 \times 10^{-7}$); thus, the four bacterial species produced MVs with different distributions of physical characteristics. The *E. coli* MV ϕ_{cal} distribution ranged from 1.5 to 4.5 with three peaks, as described in the previous section (Fig. 5a). The *P. aeruginosa* ϕ_{cal} distribution revealed two peaks centered on 1.5 and 2.6 (Fig. 5b), whereas the *P. denitrificans* (Fig. 5c) and *B. subtilis* (Fig. 5d) ϕ_{cal} values exhibited broad distributions ranging from 1 to 5 and from 1 to 4, respectively. The percentages of adherent/soft MVs (ϕ_{cal} value greater than 3) were 38%, 3.8%, 21%, and 15% for *E. coli*, *P. aeruginosa*, *P. denitrificans*, and *B. subtilis*, respectively. *E. coli* produced more adherent/soft MVs than the other bacterial species. In contrast, the percentages of nonadherent/hard MVs (ϕ_{cal} value of less than 2) were 13%, 47%, 34%, and 55% for *E. coli*, *P. aeruginosa*, *P. denitrificans*, and *B. subtilis*, respectively. *P. aeruginosa* and *B. subtilis* produced more nonadherent/hard vesicles than the other two bacterial species.

Discussion

We developed a method to quantitatively measure the physical properties of individual nanometer-scale fragile MVs under physiological conditions using high-speed AFM phase imaging. Phase imaging does not require staining, labelling, or chemical fixation, which may damage specimens. Moreover, in contrast to conventional AFM, high-speed AFM is dedicated to observing soft biological materials, proteins, and living cells. Our results reveal that high-speed AFM phase imaging is a suitable technique for MV observation and is a promising platform for analyzing the physical properties of individual MV particles in their native state.

Here, we demonstrated that a single bacterial species generates physically heterogeneous types of MVs (Fig. 4). Furthermore, we found that different bacterial species form MVs with different distributions of physical properties (Fig. 5). These findings shed light on a novel aspect of MV diversity and heterogeneity while providing insight on MV functional diversity. Previous physicochemical characterizations of bacterial MVs were mainly conducted using bulk MV mixtures. For example, sizes[33,34], zeta potentials[35,36], densities[37], and chemical[38–41] and proteinaceous[42–44] components have been estimated in bulk. Because the resulting data showed the averaged collective MV characteristics, the characteristics of each MV particle remained undetermined, and the diversity of MVs remained unknown.

Previously, the physical properties of individual eukaryotic extracellular vesicles (exosomes) were analysed using force-curve-based AFM. For example, Zhang et al., used force–distance (FD) curve-based AFM to classify eukaryotic extracellular vesicles, including exosomes, based on their stiffness.[45] Furthermore, Whitehead et al., examined exosomes derived from cancer cells, demonstrating a stiffness reduction specific to the malignant state.[46] However, the measurements of the physical properties by FD curve-based AFM is not less-invasive for fragile vesicles that consist of membrane. When we tried to use the FD curve-based method for the bacterial MVs, most bacterial MVs collapsed or were wiped out by the force of

the cantilever tip. In contrast, phase imaging can be achieved using a weak tapping force (~50 pN) that allows less-invasive physical analysis of MVs. Moreover, it is reported that measurement of vesicle stiffness using FD curve-based AFM is influenced by vesicle size.[47] Vorselen et al. demonstrated that this vesicle size dependent effect is caused by deformation (bending) of vesicles during FD curve measurement.[48] In contrast, MVs were not deformed by the scanning tip during our phase imaging. We found no correlation between phase-shift value and vesicle size (Fig. 4). Taken together, phase imaging is a suitable tool for less-invasive and comprehensive analysis of bacterial MV population containing a broad variety of vesicle diameters.

The spatial resolution of high-speed AFM is typically 2-3 nm in the x-y direction and ~0.1 nm in the z-direction[22]. Although the AFM spatial resolution in the x-y dimensions depends on the radius of the tip apex, the z-dimension is less affected[22]. In this study, MV diameters were measured from heights (z-dimension) of MV particle to avoid tip convolution artifacts resulting from the tip apex radius variation, tip attrition and/or contamination during AFM imaging.

In phase imaging, the phase-shift degrees from individual experiments are not directly compared, since the energy dissipation depends on the shape of the cantilever tip. In this study, the internal standards, polystyrene beads, were used for quantitative measurements of phase shift across experiments. This method can be applied to physical analyses of other nanoscale particles, e.g., exosomes and virus particles.

AFM phase imaging revealed a surprisingly high heterogeneity of MVs. Dissipative adhesion forces between the sample and AFM tip are the main source of the phase shift observed in liquid using the carbon tip.[32] Because adhesion stems from the chemical properties (components) of the sample surface, these results suggest that the chemical components of MV particles produced by a single bacterial species are themselves heterogeneous. Several possible causes for chemical component heterogeneity in MVs are raised by recent research insights. As one example, the presence of lipid domains and heterogeneous protein localizations in bacterial cells may reflect phase-shift degree variation. Recent studies have demonstrated that specialized membrane domains exist;[49] each such domain may generate MVs with a different membrane composition from those generated by other domains within the same cell. Alternatively, different pathways of MV formation and different physical states of bacterial cells forming MVs may affect the composition of MVs.[12] MVs originate from blebbing of the outer membrane[38–41] and are therefore enriched in outer-membrane proteins,[42–44] hence the moniker “outer MVs” (OMVs). Endolysin-triggered cell lysis generates outer-membrane vesicles and outer-inner MVs.[11] The heterogeneity of MVs isolated from the axenic culture of a single bacterial species may indicate compositional variations caused by differences in formation pathways. In addition, bacteria secrete extracellular matrices,[50] such as polysaccharides, which surround the cell surface; these may also affect the adhesiveness between an MV and an AFM tip.

In AFM imaging, the quantity and stability of MVs adsorbed to the mica substrate were greatly affected by the APTES solution concentration used for mica silanization. In addition, optimal APTES concentrations differed among bacterial species. Because the APTES concentration is expected to affect the strength of positive charges on the mica surface, our findings indicate that the electrostatic properties of MV surfaces differ among species (Fig. S1c). Several reports have demonstrated that species-specific, cell-to-cell communication is mediated by MVs.[11,51] To explain species-specific binding of *Buttiauxella agrestis* MVs, Tashiro et al. proposed that species-specific interaction energy is based on the zeta potential and hydrodynamic diameter of cells.[35] Our AFM observations support this theory. The strength of electrostatic interactions is critical for MV binding on the surface.

In this study, we demonstrated that quantifying physical properties of single MV particles using high-speed AFM phase imaging is a useful approach to understand detailed characteristics of individual bacterial MVs. AFM-based nanomechanical mapping methods which allows less invasive quantification of multiple parameters, such as height, elasticity and adhesion, have been developed.[52,53] It is expected that using these cutting-edge techniques for nanoscale physical mapping will contribute to provide further detailed information to undiscovered nature of bacterial MVs and elucidate molecular mechanisms supporting their functions.

Conclusions

As demonstrated by this study, AFM phase imaging enables the quantitative analysis of physical properties of an individual MV. Our technique provides a novel approach to understanding MV diversity and the molecular mechanisms of various MV-mediated functions. The proposed method can also be used to elucidate detailed characteristics of other biological extracellular fine particles, such as extracellular vesicles, including exosomes, which have been demonstrated to be highly diverse in their cargo.

Conflicts of interest

There are no conflicts to declare.

Acknowledgments

This work was supported by a JST ERATO grant (JPMJER1502) to Nobuhiko Nomura, and World Premier International Research Center Initiative (WPI), MEXT, Japan.

We thank Dr. Kana Morinaga, Yuma Susa, Marina Yasuda, and Hibiki Okuwaki (Tsukuba University, Japan) for preparing MV samples. We also thank Dr. Ryoma Nakao (National Institute of Infectious Diseases, Japan) for kindly providing us *E. coli* RN102.

References

1 S. Gill, R. Catchpole and P. Forterre, *FEMS Microbiol Rev*, 2019, **43**, 273–303.
2 C. Théry, L. Zitvogel and S. Amigorena, *Nat Rev Immunol*, 2002, **2**, 569–579.
3 A. F. Ellen, B. Zolghadr, A. M. Driessen and S. V. Albers SV, *Archaea*, 2010, **2010**, 608243.
4 C. Schwechheimer and M. J. Kuehn, *Nat Rev Microbiol*, 2015, **13**, 605–619.
5 M. Toyofuku, Y. Tashiro, Y. Hasegawa, M. Kurosawa and N. Nomura, *Adv Colloid Interface Sci*, 2015, **226**, 65–77.
6 M. Kaparakis-Liaskos and R. L. Ferrero, *Nat Rev Immunol*, 2015, **15**, 375–387.
7 E. J. Bunggulaw, W. Wang, T. Yin, N. Wang, C. Durkan, Y. Wang and G. Wang, *J Nanobiotechnology,* 2018, **16**, 81.
8 N. S. Barteneva, et al., *Biochim Biophys Acta Rev Cancer*, 2017, **1868**, 372–393.
9 H. A. Bladen and J. F. Waters, *J Bacteriol*, 1963, **86**, 1339–1344.
10 Y. M. D Gnopo, H. C. Watkins, T. C. Stevenson, M. P. DeLisa and D. Putnam, *Adv Drug Deliv Rev*, 2017, **114**, 132–142.
11 M. Toyofuku, N. Nomura and L. Eberl, *Nat Rev Microbiol*, 2019, **17**, 13–24.
12 L. Turnbull, M. et al., *Nat Commun*, 2016, **7**, 11220.
13 M. Toyofuku, K. Morinaga, Y. Hashimoto, J. Uhl, H. Shimamura, H. Inaba, P. Schmitt-Kopplin, L. Eberl and N. Nomura, *ISME J*, 2017, **11**, 1504–1509.
14 Y. F. Dufrêne, T. Ando, R. Garciá, D. Alsteens, D. Martinez-Martin, A. Engel, C. Gerber and D. J. Müller, *Nat Nanotechnol*, 2017, **12**, 295–307.
15 J. Tamayo and R. Garciá, *Langmuir*, 1996, **12**, 4430–4435.
16 S. N. Magonov, V. Elings and M. H. Whangbo, *Surf Sci*, 1997, **375**, L385–391.
17 G. Bar, Y. Thomann, R. Brandsch, H. J. Cantow and M. H. Whangbo, *Langmuir*, 1997, **13**, 3807–3812.
18 R. Garciá, R. Magerle and R. Perez, *Nat Mater*, 2007, **6**, 405–411.
19 B. Anczykowski, B. Gotsmann, H. Fuchs, J. P. Cleveland and V. B. Elings, *Appl Surf Sci*, 1999, **140**, 376–382.
20 N. F. Martínez and R. García, *Nanotechnology*, 2006, **17**, S167–172.
21 S. D. Connell and D. A. Smith, *Mol Membr Biol*, 2006, **23**, 17–28.
22 T. Uchihashi, N. Kodera and T. Ando, *Nat Protoc*, 2012, **7**, 1193–1206.
23 T. Ando, T. Uchihashi and S. Scheuring, *Chem Rev*, 2014, **114**, 3120–3188.
24 M. Rangl, L. Rima, J. Klement, A. Miyagi, S. Keller and S. Scheuring, *J Mol Biol*, 2017, **429**, 977–986.
25 T. Ando, *Biophys Rev*, 2017, **9**, 421–429.
26 R. Nakao, M. Ramstedt, S. N. Wai and B. E. Uhlin, *PloS one*, 2012, **7**, e51241.
27 B. W. Holloway, V. Krishnapillai and A. F. Morgan, *Microbiol Rev*, 1979, **43**, 73–102.
28 S. C. Baker, S. J. Ferguson, B. Ludwig, M. D. Page, O. M. Richter and R. J. van Spanning, *Microbiol Mol Biol Rev*, 1998, **62**, 1046–1078.
29 F. Kunst, et al., *Nature*, 1997, **390**, 249–256.
30 T. Morimoto, K. Ara, K. Ozaki and N. Ogasawara, *Genes Genet Syst*, 2009, **84**, 315–318.
31 M. Toyofuku, et al., *Nat Commun*, 2017, **8**, 481.
32 T. Uchihashi and T. Ando, *Appl Phys Lett*, 2006, **89**, 213112.
33 J. T. Tandberg, L. X. Lagos, P. Langlete, E. Berger, A. L. Rishovd, N. Roos, D. Varkey, I. T. Paulsen and H. C. Winther-Larsen, *PLoS One*, 2016 **11**, e0165099.
34 L. Fantappiè, M. de Santis, E. Chiarot, F. Carboni, G. Bensi, O. Jousson, I. Margarit and G. Grandi, *J Extracell Vesicles*, 2014, **3**, 24015.
35 Y. Tashiro, Y. Hasegawa, M. Shintani, K. Takaki, M. Ohkuma, K. Kimbara and H. Futamata, *Front Microbiol*, 2017, **8**, 571.
36 S. Halder, K. K. Yadav, R. Sarkar, S. Mukherjee, P. Saha, S. Haldar, S. Karmakar and T. Sen, *Springerplus*, 2015, **4**, 672.
37 A. L. Horstman and M. J. Kuehn, *J Biol Chem*, 2000, **275**, 12489–12496.
38 J. L. Kadurugamuwa and T. J. Beveridge, *J Bacteriol*, 1995, **177**, 3998–4008.
39 T. T. Nguyen, A. Saxena and T. J. Beveridge. *J Electron Microsc (Tokyo)*, 2003, **52**, 465–469.
40 C. Baysse, M. Cullinane, V. Dénervaud, E. Burrowes, J. M. Dow, J. P. Morrissey, L. Tam, J. T. Trevors and F. O'Gara, *Microbiology*, 2005, **151**, 2529–2542.
41 Y. Tashiro, A. Inagaki, M. Shimizu, S. Ichikawa, N. Takaya, T. Nakajima-Kambe, H. Uchiyama and N. Nomura, *Biosci Biotechnol Biochem*, 2011, **75**, 605–607.
42 S. J. Bauman and J. Kuehn, *Microbes Infect*, 2006, **8**, 2400–2408.
43 E. Y. Lee, et al., *Proteomics*, 2007, **7**, 3143–3153.
44 D. S. Choi, et al., *Proteomics*, 2011, **11**, 3424–3429.
45 H. Zhang, et al., *Nat Cell Biol*, 2018, **20**, 332–343.
46 B. Whitehead, L. Wu, M. L. Hvam, H. Aslan, M. Dong, L. Dyrskjøt, M. S. Ostenfeld, S. M. Moghimi and K. A. Howard, *J Extracell Vesicles*, 2015, **4**, 29685.
47 S. Wang, et al., *Langmuir*, 2016, **32**, 11230–11235.
48 D. Vorselen, F. C. MacKintosh, W. H. Roos and G. J. Wuite, *ACS Nano*, 2017, **11**, 2628–2636.
49 H. Strahl and J. Errington, *Annu Rev Microbiol*, 2017, **71**, 519–538.
50 H. C. Flemming and J. Wingender, *Nat Rev Microbiol*, 2010, **8**, 623–633.
51 L. M. Mashburn and M. Whiteley, *Nature*, 2005, **437**, 422–425.
52 S. Zhang, H. Aslan, F. Besenbacher and M. Dong, *Chem Soc Rev*, 2014, **43**, 7412–7429.
53 A. P. Nievergelt, C. Brillard, H. A. Eskandarian, J. D. McKinney and G. E. Fantner, *Int J Mol Sci*, 2018, **19**, 2984.

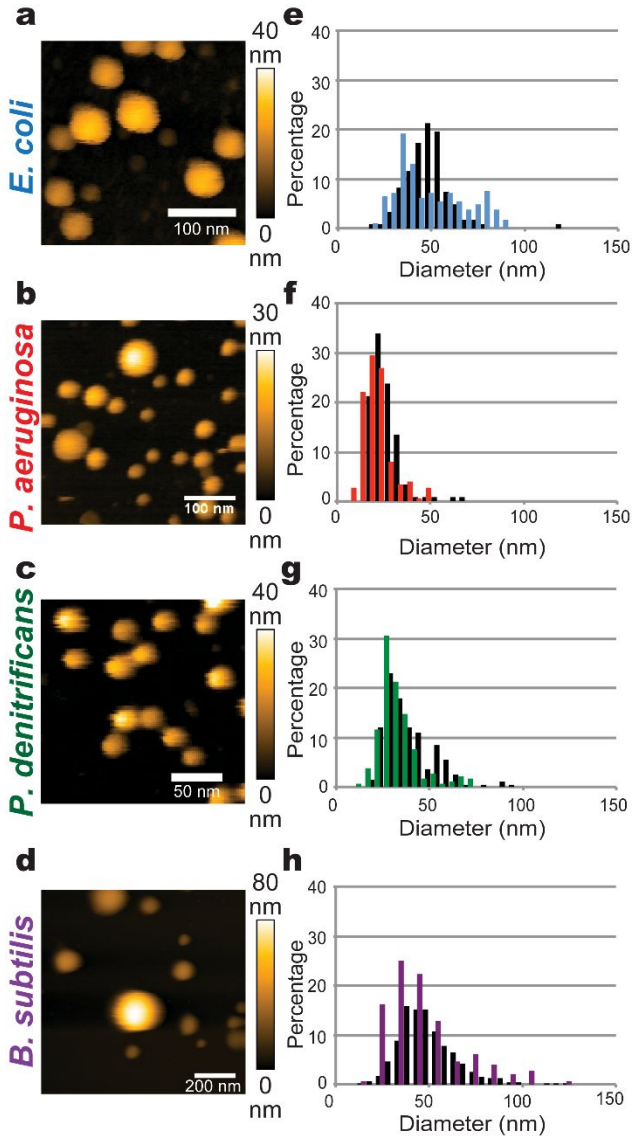

Fig. 1 AFM images and diameter distributions of bacterial MVs. (a–d) The topographic AFM images of (a) *E. coli*, (b) *P. aeruginosa*, (c) *P. denitrificans*, and (d) *B. subtilis* MVs on mica substrates in PBS. MVs were immobilized on the mica surfaces by treatment with the optimal APTES concentration (*E. coli*, 0.02%; *P. aeruginosa*, 0.05%; *P. denitrificans*, 0.03%; *B. subtilis*, 0.0001%). (e–h) The diameter distributions of (e) *E. coli*, (f) *P. aeruginosa*, (g) *P. denitrificans*, and (h) *B. subtilis* MVs measured by AFM (colored bars) and TEM (black bars). The diameter distributions of MVs imaged by AFM and TEM overlapped, indicating that all sizes of MVs within the samples could be imaged by AFM. AFM images were recorded at imaging rates of either (a–c) 2.0 s/frame and 200 × 200 pixels or (d) 5.0 s/frame and 400 × 400 pixels. White bars: (a–b) 100 nm; (c) 50 nm; (d) 200 nm.

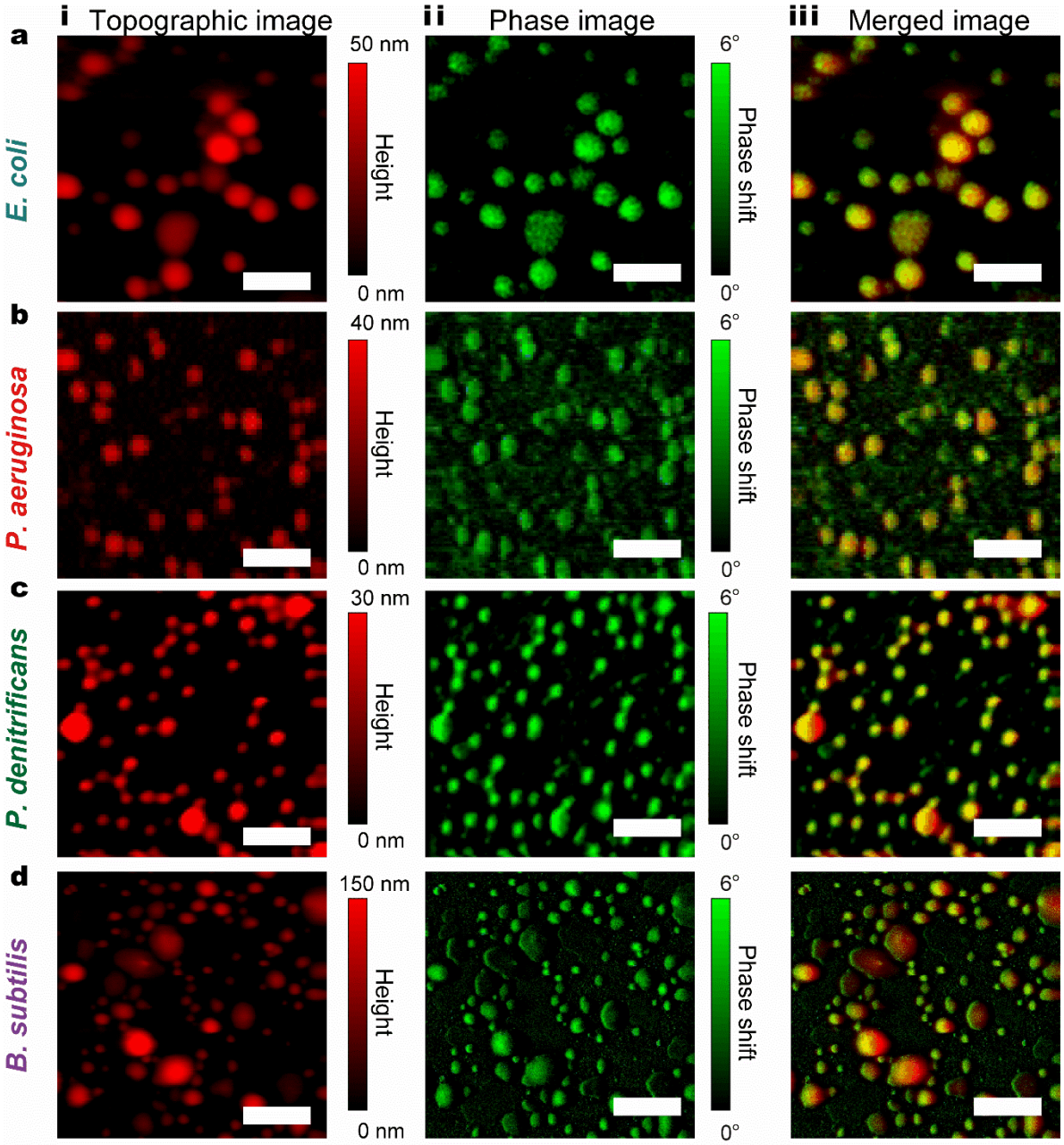

Fig. 2 Imaging of physical properties of individual MVs. The AFM topographic images (Column i) and phase images (Column ii) of MVs were acquired simultaneously for (a) *E. coli*, (b) *P. aeruginosa*, (c) *P. denitrificans*, and (d) *B. subtilis*. Column iii presents the merged images of the topographic and phase images. The merged images exhibit nonadherent/hard MVs as reddish particles and adherent/soft MVs as greenish particles. The variety in MV colors indicates physical heterogeneity among bacterial MVs. AFM images were recorded at imaging rates of either (a–c) 2.0 s/frame and 200 × 200 pixels or (d) 5.0 s/frame and 400 × 400 pixels. White bars: (a–c) 100 nm; (d) 200 nm.

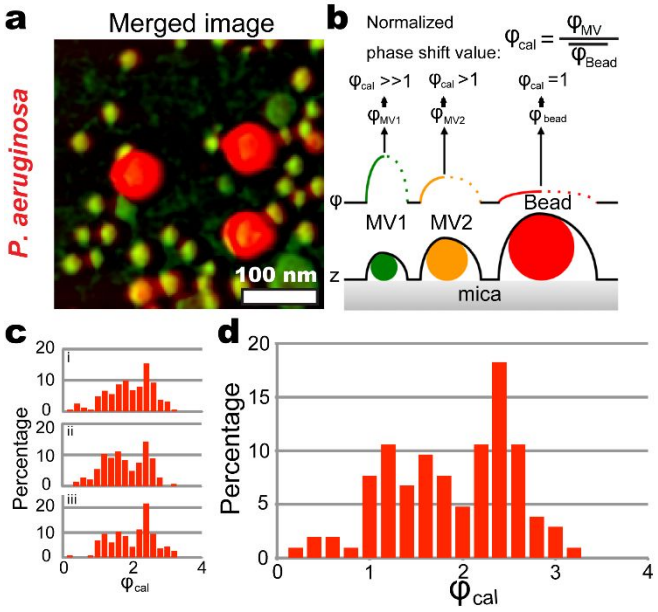

Fig. 3 Quantitative physical analysis of individual MVs. (a) The merged image of the topographic and phase images of *P. aeruginosa* MVs and polystyrene beads. AFM images were recorded at imaging rates of 2.0 s/frame and 200 × 200 pixels. (b) Schematic diagram of AFM observation of MVs and polystyrene beads. The colors of MV1, MV2, and beads represent those in the merged image (panel a). MV1 (green) and MV2 (orange) represent adherent/soft and nonadherent/hard MVs, respectively. Red indicates polystyrene beads with nonadhesive, hard surfaces. The height (z) and the phase-shift degree (ϕ) of samples were recorded by the scanning of the cantilever from left to right. The topographic image (black line) of the sample structure was extended horizontally by the radius of the cantilever tip. The ϕ values differed on the left side and right side of the top of the particles due to parachuting of the cantilever (Fig. S5). The phase-shift degree obtained at the top of each MV (ϕ_{MV}) or polystyrene bead (ϕ_{bead}) was used in order to avoid artifacts from parachuting. The formula for the calculation of ϕ_{cal} is presented. (c) The *P. aeruginosa* MVs ϕ_{cal} distribution obtained from three independent experiments (i–iii). The bin width was 0.2. (d) The histogram of *P. aeruginosa* MV ϕ_{cal} values obtained by cumulating the results in panel c (*n* = 154).

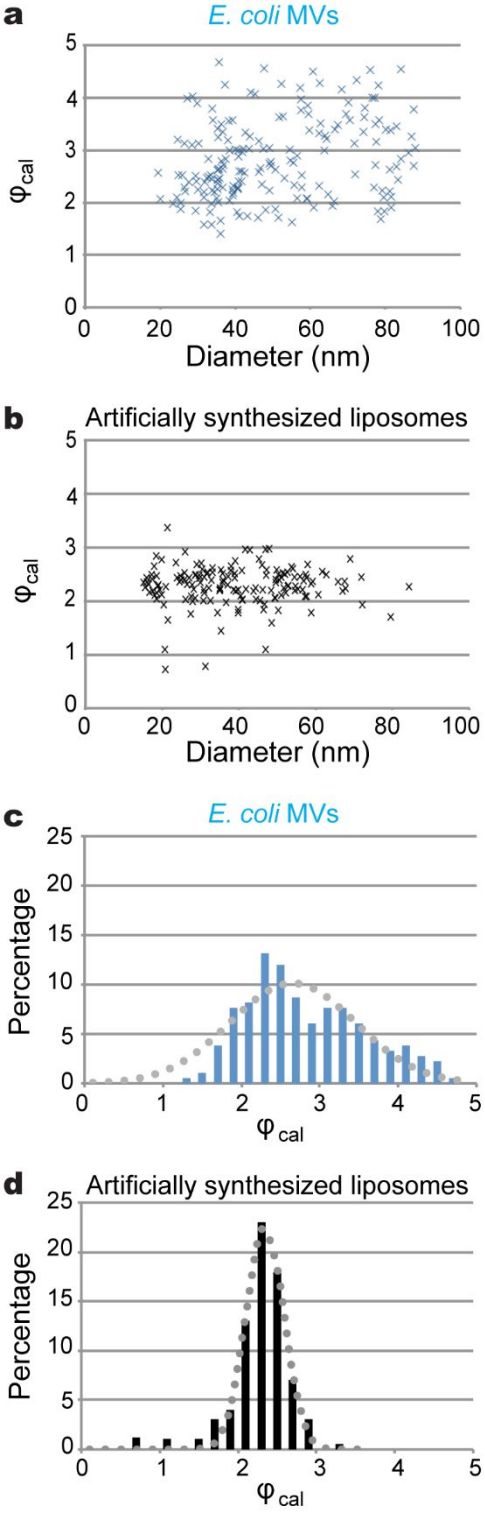

Fig. 4 Comparison of the ϕ_{cal} distributions for *E. coli* MVs and liposomes. Scatterplots of ϕ_{cal} value versus diameter for (a) *E. coli* MVs and (b) artificially synthesized liposomes. (c) *E. coli* MV ϕ_{cal} distribution (n = 183) and (d) liposome ϕ_{cal} distribution (n = 123) estimated from three independent measurements. The dashed lines indicate fitted Gaussian curves. The liposome ϕ_{cal} distribution did not fail to fit the Gaussian curve (p = 0.93), whereas the *E. coli* MV ϕ_{cal} distribution did fail to fit (p < 0.005).

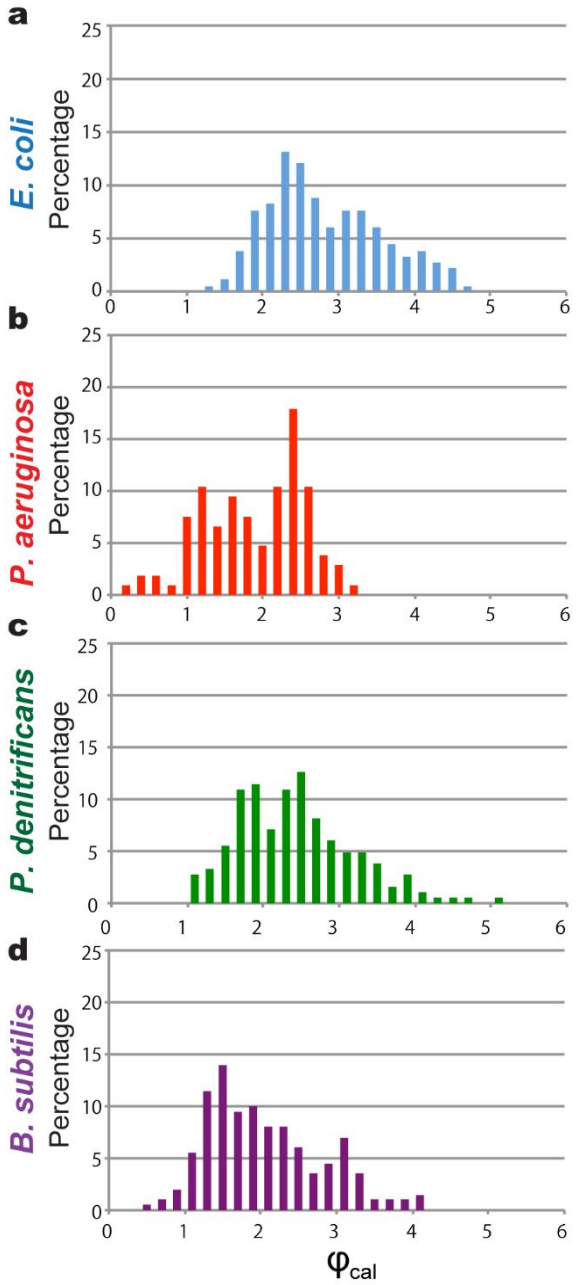

Fig. 5 Species-specific ϕ_{cal} distributions of bacterial MVs. MV ϕ_{cal} distributions from the four bacterial species: (a) *E. coli* (n = 183), (b) *P. aeruginosa* (n = 154), (c) *P. denitrificans* (n = 192), (d) *B. subtilis* (n = 287). Each result was estimated from (a–c) three or (d) four independent measurements. The bin width was 0.2. MVs exhibited heterogeneous distributions in each bacterial species. The ϕ_{cal} distributions of different bacterial species differed significantly ($p < 1\times10^{-7}$).

This study provides a new methodology using the phase imaging for quantitative single-vesicle physical characterization of extracellular bacterial membrane vesicles.

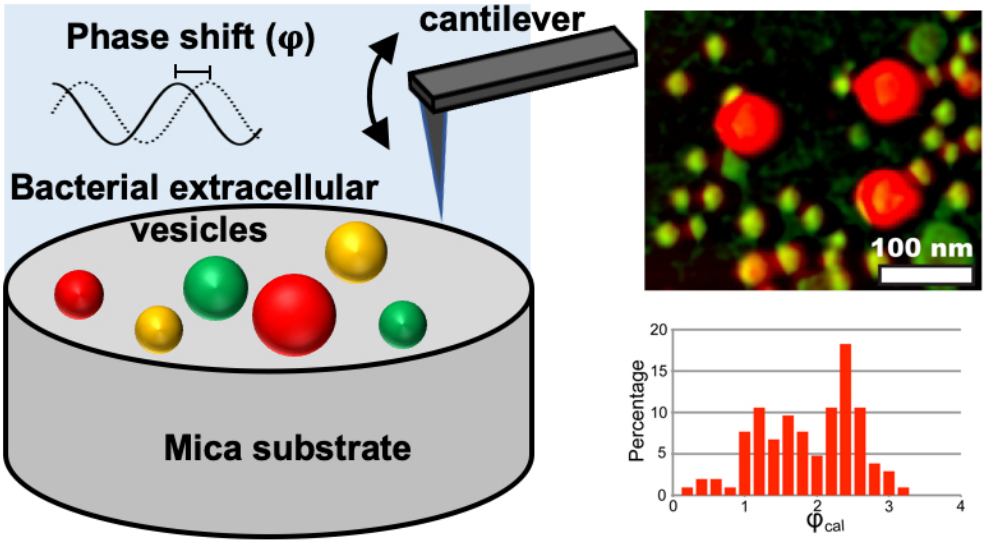

69x39mm (285 x 285 DPI)